catalysts

MDPI

Article

One-Pot Phyto-Mediated Synthesis of Fe_2O_3/Fe_3O_4 Binary Mixed Nanocomposite Efficiently Applied in Wastewater Remediation by Photo-Fenton Reaction

Amr A. Essawy [1,*], Tamer H. A. Hasanin [1], Modather. F. Hussein [1], Emam F. El Agammy [2] and Abd El-Naby I. Essawy [3]

[1] Chemistry Department, College of Science, Jouf University, Sakaka P.O. Box 72341, Aljouf, Saudi Arabia
[2] Physics Department, College of Science, Jouf University, Sakaka P.O. Box 72341, Aljouf, Saudi Arabia
[3] Chemistry Department, Faculty of Science, Fayoum University, Fayoum 63514, Egypt
* Correspondence: aaessawy@ju.edu.sa

Abstract: A binary Fe_2O_3/Fe_3O_4 mixed nanocomposite was prepared by phyto-mediated avenue to be suited in the photo-Fenton photodegradation of methylene blue (MB) in the presence of H_2O_2. XRD and SEM analyses illustrated that Fe_2O_3 nanoparticles of average crystallite size 8.43 nm were successfully mixed with plate-like aggregates of Fe_3O_4 with a 15.1 nm average crystallite size. Moreover, SEM images showed a porous morphology for the binary Fe_2O_3/Fe_3O_4 mixed nanocomposite that is favorable for a photocatalyst. EDX and elemental mapping showed intense iron and oxygen peaks, confirming composite purity and symmetrical distribution. FTIR analysis displayed the distinct Fe-O assignments. Moreover, the isotherm of the developed nanocomposite showed slit-shaped pores in loose particulates within plate-like aggregates and a mesoporous pore-size distribution. Thermal gravimetric analysis (TGA) indicated the high thermal stability of the prepared Fe_2O_3/Fe_3O_4 binary nanocomposite. The optical properties illustrated a narrowing in the band gab (Eg = 2.92 eV) that enabled considerable absorption in the visible region of solar light. Suiting the developed binary Fe_2O_3/Fe_3O_4 nanocomposite in the photo-Fenton reaction along with H_2O_2 supplied higher productivity of active oxidizing species and accordingly a higher degradation efficacy of MB. The solar-driven photodegradation reactions were conducted and the estimated rate constants were 0.002, 0.0047, and 0.0143 min^{-1} when using the Fe_2O_3/Fe_3O_4 nanocomposite, pure H_2O_2, and the $Fe_2O_3/Fe_3O_4/H_2O_2$ hybrid catalyst, respectively. Therefore, suiting the developed binary Fe_2O_3/Fe_3O_4 nanocomposite and H_2O_2 in photo-Fenton reaction supplied higher productivity of active oxidizing species and accordingly a higher degradation efficacy of MB. After being subjected to four photo-Fenton degradation cycles, the Fe_2O_3/Fe_3O_4 nanocomposite catalyst still functioned admirably. Further evaluation of Fe_2O_3/Fe_3O_4 nanocomposite in photocatalytic remediation of contaminated water using a mixture of MB and pyronine Y (PY) dyestuffs revealed substantial dye photodegradation efficiencies.

Keywords: phytosynthesis; hematite/magnetite nanocomposite; solar photocatalysis; photo Fenton reaction; wastewater remediation

Citation: Essawy, A.A.; Hasanin, T.H.A.; Hussein, M.F.; El Agammy, E.F.; Essawy, A.E.-N.I. One-Pot Phyto-Mediated Synthesis of Fe_2O_3/Fe_3O_4 Binary Mixed Nanocomposite Efficiently Applied in Wastewater Remediation by Photo-Fenton Reaction. *Catalysts* **2024**, *14*, 466. https://doi.org/10.3390/catal14070466

Academic Editors: Elisabete C.B.A. Alegria and Bo Weng

Received: 30 May 2024
Revised: 18 July 2024
Accepted: 18 July 2024
Published: 20 July 2024

1. Introduction

Water contamination is one of the most urgent environmental problems we face today. Products containing dyes are an example of hazardous industrial waste. If that is the case, the water cannot simply be dumped into water bodies; it is necessary that the contaminants are first removed or chemically decomposed [1]. Meanwhile, human activities and the quantity of energy used to power those endeavors have both increased dramatically. Reducing energy consumption and the associated negative effects on the environment can be achieved through the use of sustainable alternatives, for example, using natural sources [2]. As a result, there is an urgent need for the design of practical

wastewater treatment systems that use less power. Sunlight-driven photocatalysis is an important green technology in this context because it allows for the safe and inexpensive elimination of toxic organic pollutants. As far as advanced oxidation technologies (AOPs) go, photocatalysis and Fenton reactions utilizing transition metal oxides are the most cutting-edge methods for cleaning up wastewater. These AOPs function in a wide range of conditions, employ various mechanisms, and are appealing for a number of reasons, including superior stability, facile-driven conditions, reasonable price, and reusability [3,4]. The most interesting and promising of these transition metal oxides were iron oxides, which had special properties like being cheap, easy to separate at the end of the reaction for later use because they are magnetic, have an appropriate band gap, and are chemically stable [5]. Most of the iron oxide minerals that are found are hematite (α-Fe_2O_3), maghemite (γ-Fe_2O_3), and magnetite (Fe_3O_4). Chemically produced nanosized iron oxides showed strong decomposition abilities for a wide range of organic dyes [6,7].

Unfortunately, photocatalysis is insufficiently effective for the remediation of highly concentrated and nontransparent dyes because light has a limited penetrating capacity [3,8]. Heterogeneous Fenton catalysis can be used to circumvent this shortcoming. A wide variety of inorganic compounds can be oxidized via Fenton reactions due to the presence of nonselective active species [9]. Heterogeneous photocatalysis actually makes it possible to harness the sun's energy without resorting to fossil fuels. The Fenton oxidation method is a famous and well-studied example of a technique for treating wastewater. Magnetite [10], ferrihydrite [11], and hematite [12] are the most studied and straightforward examples of Fenton-like oxidation reactions.

Single-metal oxide solar photocatalysts, however, have lower photocatalytic efficacy because charge recombination is not favored. Water purification, antibacterial effectiveness, water splitting, and carbon dioxide reduction are all examples of photocatalytic applications where the stability of structuralism and quantum effectiveness can be improved by obtaining a heterojunction system via the coupling of metal oxides [13]. Recently, the industrial waste iron oxide dust composed of α-Fe_2O_3 was chemically reduced, producing Fe_3O_4@α-Fe_2O_3, which showed an improved response to visible light for the enhanced photodegradability of dyes [14] and the solar-driven photoreduction of hexavalent chromium (Cr(VI)) from aquatic media [15]. In addition, various synthesis methods, including solvothermal, solid-state, hydrothermal, and solution combustion techniques, can be used to create these composites. In contrast to physical and chemical methods, plant extract-mediated synthesis of metal nanoparticles currently offers a green, practical, and simple methodology [16,17].

Dye degradation is aided by hydroxyl radicals ($^{\bullet}OH$), which are produced as a byproduct of the photo-Fenton reaction, in which H_2O_2 is catalytically reacted with iron ions in the presence of light [18]. With the goal of increasing the reaction rate and the yield of mineralization, a modern strategy involving the utilization of a hybrid system consisting of a heterojunction photocatalyst along with a heterogeneous photo-Fenton approach has proven to be very fruitful [19,20]. The photo-Fenton process is superior to either process alone for degrading organic pollutants due to the synergistic influence of photo-Fenton and photocatalysis. Increased interest in these techniques [21,22] can be attributed to the fact that iron nanoparticles with peroxidase-like activity improve Fenton properties by activating H_2O_2 for a high mineralization yield.

MB is a versatile chemical that has many applications in the pharmaceutical, aquaculture, and synthesis industries. One of the xanthene dyes is pyronin Y (PY), which is a water-soluble chromogen that is currently used as an optical probe for the assaying of glucose in human serum and uric acid/formaldehyde in blood plasma. It was successfully degraded over surfaces of titania-mixed cement composites under UV illumination [23]. Exposure to polluted water could raise some of the possible symptoms, like vomiting, bladder inflammation, abdominal discomfort, and excessive urination [24].

In this work, we developed a facile one-pot green approach to synthesize binary Fe_2O_3/Fe_3O_4 mixed nanocomposite that is highly efficacious in absorbing solar light as a readily accessible and sustainable natural source of energy in waste water treatment

for the cleanup of organic contaminants. The structural, morphological, and optical characteristics were addressed. The photocatalytic efficacy of the synthesized Fe_2O_3/Fe_3O_4 nanocomposite was tested for degradation of MB along with PY in aqueous solutions. The photocatalytic efficacy of the synthesized Fe_2O_3/Fe_3O_4 nanocomposite was firstly examined in the photo-Fenton degradation of pure MB in aqueous solution at natural pH under solar illumination. Then, the solar-driven photo-Fenton degradation efficacy of the developed nanocomposite was further tested for degradation of MB along with PY that were spiked in real lake water samples.

2. Results and Discussion

2.1. X-ray Diffraction (XRD)

A comparative powder XRD analysis was employed to identify the composition, phase purity and crystal lattice of the developed iron oxide sample. As seen in Figure 1A, the XRD data of the developed iron oxide revealed intense diffraction peaks allocated at 2θ = 30.2, 35.6, 43.4, 53.8, 57.4, 63, and 74.4o that could be indexed to the (220), (311), (400), (422), (511), (440), and (533) planes, respectively, corresponding to the cubic phase of Fe_3O_4 [25]. This is in agreement with the standard value of Fe_3O_4 (JCPDS file no: 65-3107). In addition, three diffraction peaks of lower intensity were depicted at 2θ = 33, 40.8, and 49.6o that could be indexed to the (104), (113), and (024) planes of Fe_2O_3 [13]. The mean crystallite size of the obtained Fe_2O_3 and Fe_3O_4 particulates was calculated based on the full width at half-maximum (FWHM) and the Debye–Sherrer formula, the following equation has been derived: $D = K\lambda/\beta \cos\theta$, where θ is the Bragg angle, K is the shape factor of value 0.89, λ is the X-ray wavelength, and β is the FWHM line broadening in radians. The average size of Fe_2O_3 was around 8.43 nm while that of Fe_3O_4 was markedly greater with an estimate amounting to 15.1 nm.

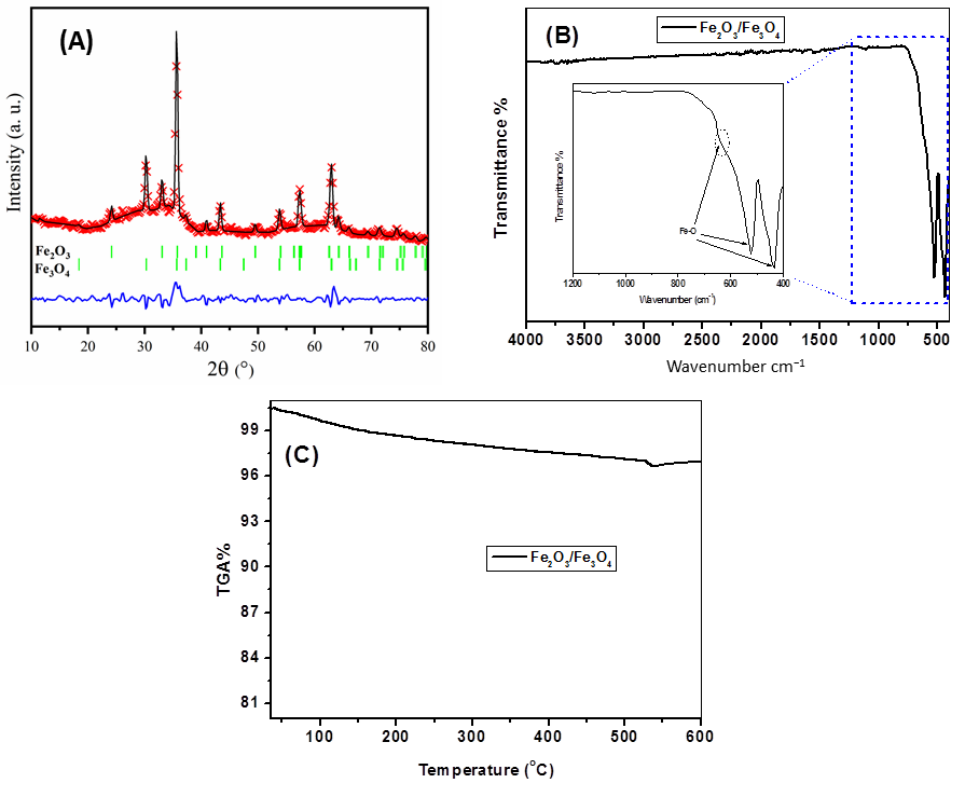

Figure 1. XRD pattern with Rietveld refinement. (**A**) FTIR spectrum; (**B**) TGA profile; (**C**) of the developed binary Fe_2O_3/Fe_3O_4 nanocomposite.

2.2. Fourier Transform Infrared (FTIR) Characterization

The FTIR spectrum of the developed binary-mixed Fe_2O_3/Fe_3O_4 NPs was measured (Figure 1B). Two prominent peaks, at 524.1 and 432.6 cm^{-1}, in addition to a shoulder assigned at 624 cm^{-1}, are displayed. Oxygen bonds with metal cations (Fe-O stretching) are responsible for these intrinsic stretching vibrations [26–28] referring to the A_{2u}/E_u vibrational overlap with the dipolar moments that are parallel to and perpendicular to the c axis which is specified in hematite [29] along with the IR active T_{1u} mode characteristic for magnetite [30]. While the assigned shoulder at 624 cm^{-1} is due to the symmetry degeneration on octahedral B-sites [30].

2.3. Thermal Gravimetric Analysis (TGA)

TGA was performed to ascertain the thermal stability of the newly phyto-synthesized Fe_2O_3/Fe_3O_4 binary nanocomposite. Figure 1C shows the TGA thermogram of Fe_2O_3/Fe_3O_4 binary nanocomposite. The results indicated a slight weight loss of about 0.96% at ≈139 °C that could be attributed to some adsorbed water content. While the subsequent incremental temperature till reaching 600 °C further accompanied by weight loss of about 2.16% that can be correlated to the breakdown of biomolecules, such as phenolics and flavonoids, that were left over after the developed phyto-synthetic avenue. This indicates high thermal stability of the prepared Fe_2O_3/Fe_3O_4 binary nanocomposite.

2.4. Scanning Electron Microscopy (SEM) Characterization

The surface morphology of the developed Fe_2O_3/Fe_3O_4 nanocomposite was studied using SEM analysis. Figure 2A displays a dominant of an assemblage of irregularly coarse plate-like shaped Fe_3O_4 nanoparticles that are adorned with very fine Fe_2O_3 particulates. The observed irregular and porous construction is suggestive of the successful adorning and hetero-structuralism of Fe_2O_3 and Fe_3O_4. This porous morphology is advantageous for photodegradation because it increases the contact surface area and absorbs more light which enhances the photodegradation efficiency [31].

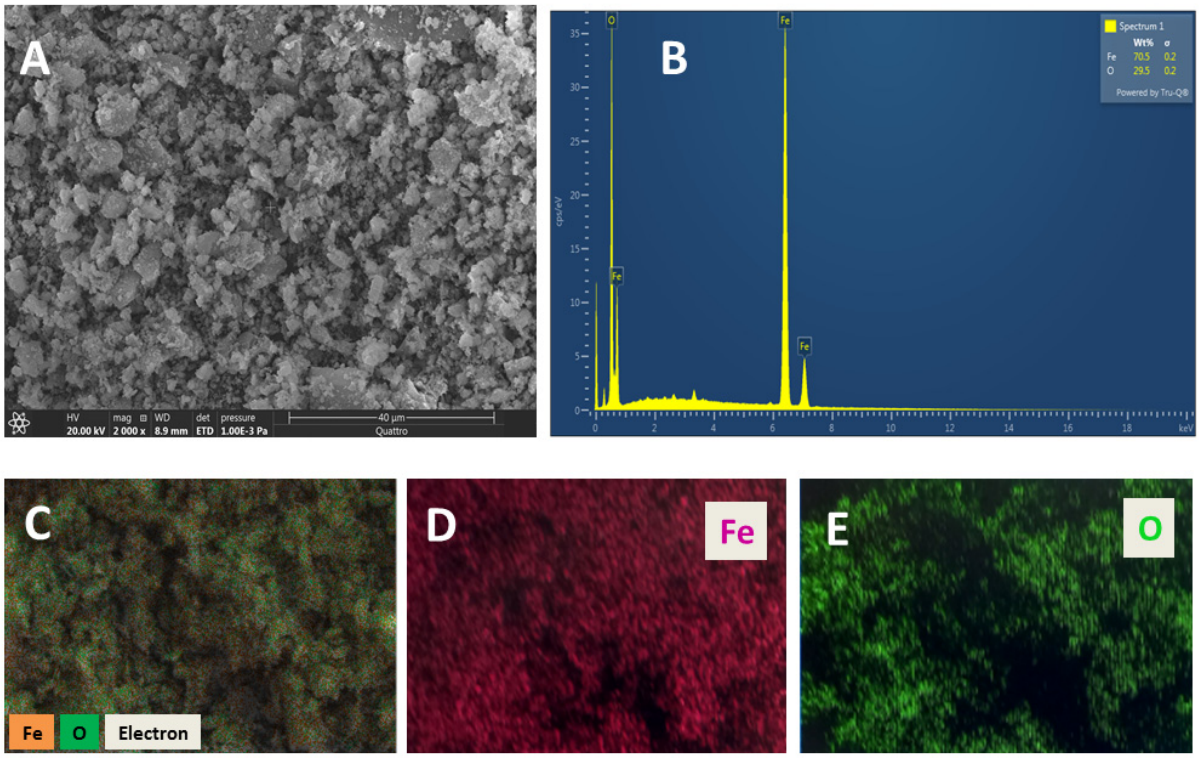

Figure 2. SEM image. (**A**) EDX spectrum; (**B**) EDS mapping; (**C**–**E**) of the developed binary Fe_2O_3/Fe_3O_4 nanocomposite.

Energy-dispersive X-ray (EDX) and elemental mapping were analyzed to characterize the elements Fe and O in the developed nanocomposite to better address their content and distribution. The EDX spectrum shown in Figure 2B illustrates highly intense peaks of iron, and oxygen verifying that the developed composite of iron oxide nanoparticle was of the highest purity. Moreover, the EDX analysis in Figure 2B shows that the percentage of Fe and O were found to be 70.5% and 29.5%, respectively, confirming that there are no other elements besides Fe and O in the composite. As seen from the elemental mapping (Figure 2C–E), the iron distribution (red coloration) and the oxygen distribution (green coloration) are highly symmetrical and uniform.

Contemplating the results revealed from XRD, FTIR, SEM, and EDS analyses indicate that the developed iron oxide sample is a binary Fe_2O_3/Fe_3O_4 nanocomposite in which the minor Fe_2O_3 adorned the massive Fe_3O_4 particulates.

2.5. Textural Features

The N_2 adsorption–desorption measurements (Figure 3) were used to evaluate the textural properties of the heterostructure Fe_2O_3/Fe_3O_4 nanocomposite. As seen in Figure 3A, the depicted isotherm exhibited a hysteresis loop from which the shape of the pore structures could be inferred [32]. The isotherm has characteristics typical of slit-shaped pores within loose particulates in plate-like aggregates, so it may be classified as type IV with a type H3 hysteresis loop [33]. The morphological characteristics addressed by the SEM imaging are consistent with these findings. The pore size distribution was illustrated in Figure 3B that signifies distinct peaks in the mesoporous range (2–50 nm). Additionally, the surface area calculation using BET equation yields an estimate of 41.45 m^2g^{-1}. Therefore, the one-pot biogenic-mediated reaction exhibits high quality and meets all requirements in terms of larger pore volumes as well as higher specific surface areas, conducing for a large number of surface active sites [34]. These features are greatly demanded for efficient performance of photocatalysts.

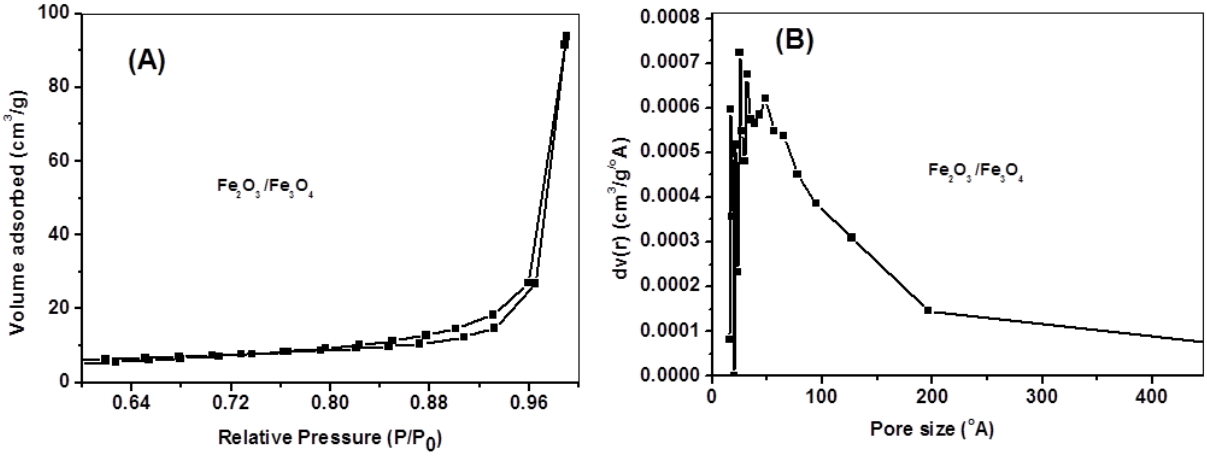

Figure 3. N_2 adsorption–desorption isotherm (**A**) and pore size distribution (**B**) of the developed binary Fe_2O_3/Fe_3O_4 nanocomposite.

2.6. UV-Vis Spectroscopy and Calculations of Band Gab

Nanostructure materials' utility in fields like optoelectronics and photocatalysis is largely determined by their optical energy gap (E_g) [35,36]. Ultraviolet/visible absorption spectroscopy measurements are performed between 200 and 800 nm to calculate the optical energy gap for the developed binary Fe_2O_3/Fe_3O_4 nanocomposite. Figure 4A shows the electronic excitation spectra of the synthesized binary Fe_2O_3/Fe_3O_4 nanocomposite. As seen, the absorption spectrum recorded an absorption maxima at 400 nm and a shoulder at 290 nm in addition to tailing off of considerable absorption in the visible region. This anticipates a narrow band gab and efficient absorptivity of solar light.

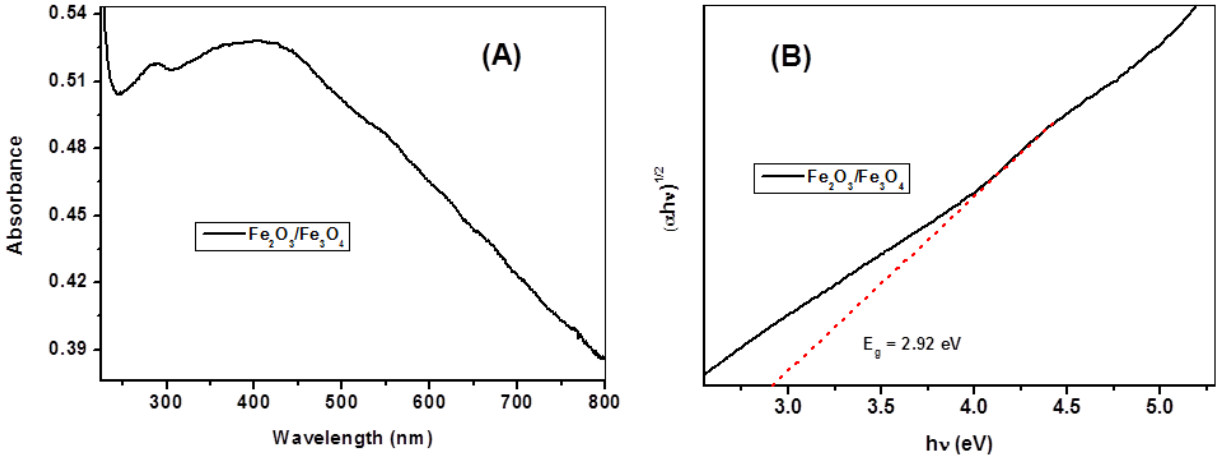

Figure 4. UV–Visible electronic spectra of Fe_2O_3/Fe_3O_4 nanocomposite (**A**) and the corresponding plot of $(\alpha h\upsilon)^{1/2}$ versus $h\upsilon$ (**B**).

Otherwise, Figure 4B shows Kubelka–Munk function plotting (Equation (1)) to determine the band gap of the developed Fe_2O_3/Fe_3O_4 nanocomposite.

$$\alpha h\upsilon = A\,(h\upsilon - E_g)^{1/2} \quad (1)$$

where h is the Planck constant; α is the extinction coefficient; A is the absorption constant; υ is the frequency of vibration; and E_g is the energy gap in eV. The estimated value of E_g for Fe_2O_3/Fe_3O_4 nanocomposite is 2.92 eV based on the linear extrapolating of $(\alpha h\upsilon)^{1/2}$ relative to $(h\upsilon)$. The band gap of a material is influenced by its crystal structure and the size of its particles. An additional critical factor influencing the materials' optical properties is the shape-dependent effect, which arises from the possibility of orientation along a single axis. According to the literature, the band gaps of Fe_2O_3 and Fe_3O_4 are about 2.15 eV and 2.4 eV, respectively [37,38].

2.7. Photo-Fenton Activity of the Constructed Binary Fe_2O_3/Fe_3O_4 Nanocomposite

MB was selected as a model pollutant to assess the photodegradation efficacy of the developed catalysts using Equation (2) [35]:

$$E\% = \frac{A_0 - A_t}{A_0} \times 100 \quad (2)$$

where E% denotes the photodegradation efficacy for MB removal; A_0 represents the highest MB absorbance (λ_{max} 663 nm) before running irradiation process; and A_t denotes the absorbance measured at specified illumination time (t).

Prior to the MB illumination in the presence of various catalysts, 30 min of contacting the catalysts with MB discloses a weak adsorption-based MB removal process. Furthermore, Figure 5A depicts the temporal correlated monitoring of MB absorption profile in presence of the $Fe_2O_3/Fe_3O_4/H_2O_2$ hybrid catalyst.

Applying the equation of first-order kinetics [39,40] with depiction of $\ln(A/A_0)$ versus illumination time (t), as shown in Figure 5B, revealed good linear fitting ($r^2 > 0.9$). The rate constants of the photodegradation reactions are 0.002, 0.0047, and 0.0143 min^{-1} when using Fe_2O_3/Fe_3O_4 nanocomposite, pure H_2O_2, and the $Fe_2O_3/Fe_3O_4/H_2O_2$ hybrid catalyst, respectively. Therefore, the latter improved the photocatalytic degradation of MB by 3.04 folds when compared to the usage of H_2O_2 homogenous catalyst while it was by 7.15 folds of improving MB photodegradation compared to the usage of pure Fe_2O_3/Fe_3O_4. These results illustrate the synergism between the developed Fe_2O_3/Fe_3O_4 nanocomposite and H_2O_2 in suiting the photo-Fenton reactions that supply higher productivity of active oxidizing species and accordingly higher degradation efficacy (Figure 6A). The optimal

conditions for the photo-Fenton reaction and the degradation% of MB under various irradiation sources and catalysts are compared in Table 1. When compared to other reported photocatalysts [41–44], the Fe_2O_3/Fe_3O_4 nanocomposite synthesized in this study stands out as particularly effective with higher efficacy under solar irradiation compared to bulb light illumination. This is reasonable as sunlight has a wide spectrum from UV to NIR that plays a dual role in exciting the photoactive Fe_2O_3/Fe_3O_4 nanocomposite and offering a temperature that is appropriate for increasing the rate of photodegradation [45,46]. The Fe_3O_4 particles fared better than the Fe_2O_3 ones in the photo-Fenton process. There were more ferrous ions than Fe(III) ions in the magnetite material, and the Fe(II) ions were able to strongly facilitate the photo-Fenton reaction. Also, unlike the conventionally used lower pH with other catalysts, our study achieved a considerable percentage of MB removal in an aqueous solution at its natural pH 7.1. Moreover, the present study utilizes a smaller amount of catalyst, but it is easily separated with a magnet to be reused in consecutive runs of photo-Fenton reaction within efficient performance. The effectiveness of the Fe_2O_3/Fe_3O_4 nanocomposite in the solar-driven photo-Fenton mineralization of MB was further evaluated using TOC measurements. The initial TOC measurement of MB at zero solar illumination recorded 19.3 ppm and decreased to 5.7 ppm after 75 min of illumination.

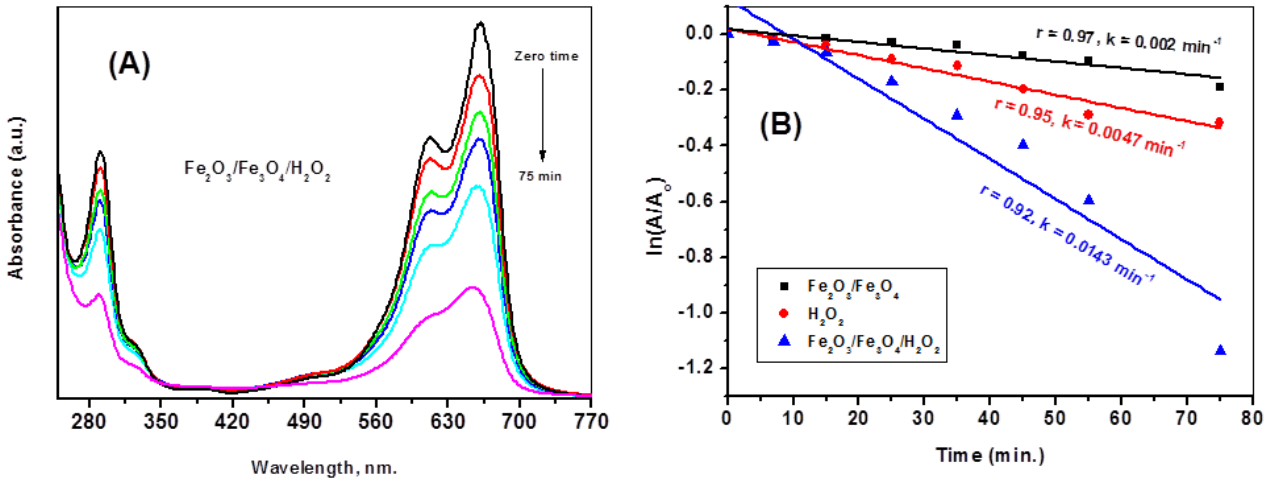

Figure 5. Time-dependent variations in absorption spectrum of MB during the solar-driven photo-Fenton catalytic degradation in presence of $Fe_2O_3/Fe_3O_4/H_2O_2$ hybrid catalyst (**A**) and the first order photodegradation kinetics for detoxification of MB using Fe_2O_3/Fe_3O_4, H_2O_2, and $Fe_2O_3/Fe_3O_4/H_2O_2$ catalysts (**B**).

Table 1. Comparison of the catalytic performance in the removal of MB after photodegradation reactions using different catalysts.

Sample	Synthetic Route	mcat (g L^{-1})	pH	[MB] (mg L^{-1})	Removal% or Degradation Rate (min^{-1})	Irradiation	Ref
Fe_3O_4-RGO	Green method (*Sargassum thunbergii* alga)	0.25	6.0	34	17%	300 W (Xenon lamp)	[41]
α-Fe_2O_3-GO	Chemical hydrolysis (Urea-reducing agent)	0.25	3.0	37	65%	100 W (Mercury lamp)	[42]
Fe_3O_4-ZeoliteA	Chemical method (Post-precipitation)	0.4	3.0	17	32%	6 W (UV-C lamp)	[43]

Table 1. *Cont.*

Sample	Synthetic Route	mcat (g L^{-1})	pH	[MB] (mg L^{-1})	Removal% or Degradation Rate (min^{-1})	Irradiation	Ref
$LaFeO_3$ $LaFe_{0.9}Ni_{0.1}O_3$ $LaFe_{0.7}Ni_{0.3}O_3$ $LaFe_{0.5}Ni_{0.5}O_3$	Sol–gel	0.33	7	133	0.0086 min^{-1} 0.003 min^{-1} 0.0039 min^{-1} 0.002 min^{-1}	simulated AM 1.5G solar light	[44]
Fe_2O_3/Fe_3O_4	Biogenic method (guajava leaves extract)	0.20	7.1	20	71.9% 0.0143	Sun light (760 W/m^2)	This work
Fe_2O_3/Fe_3O_4	Biogenic method (guajava leaves extract)	0.20	7.1	20	54.7% 0.0102	Bulb light (100 W)	This work

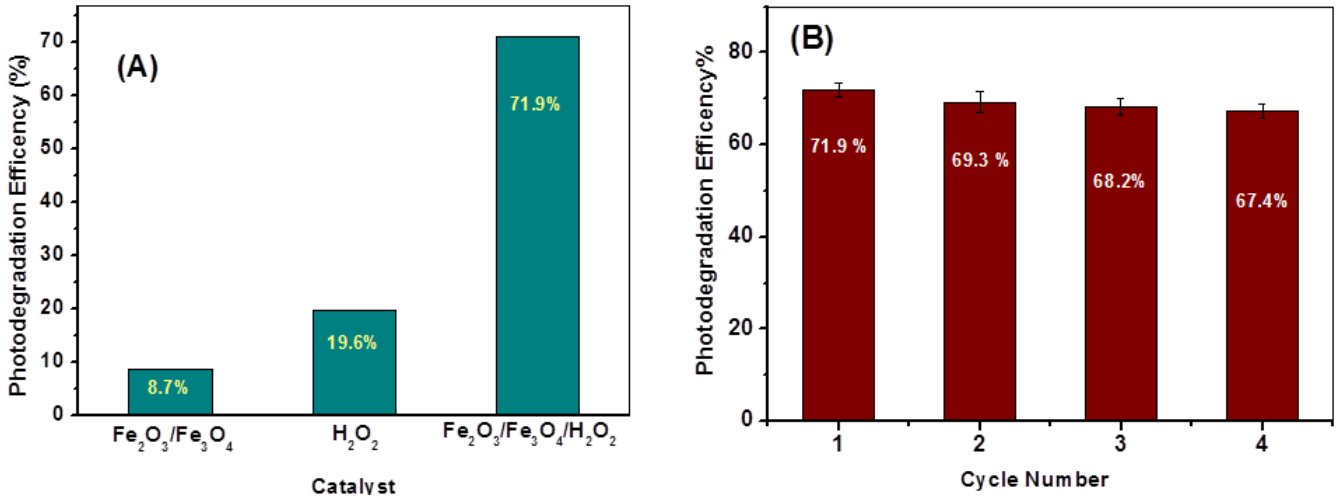

Figure 6. Comparison of MB photodegradation in presence of Fe_2O_3/Fe_3O_4, H_2O_2, and $Fe_2O_3/Fe_3O_4/H_2O_2$ catalysts. (**A**) The durability study of the developed heterostructure during consecutive cycles of photo-Fenton processes (**B**).

If catalysts are to have any practical applicability, the ability to reuse the catalytic materials is essential. Four consecutive cycles of photo-Fenton reactions start with 0.2 g L^{-1} of Fe_2O_3/Fe_3O_4 nanocomposite and in each run, 20 mg L^{-1} of H_2O_2 and 20 mg L^{-1} of MB was added which showed that MB could be degraded effectively. Figure 6B demonstrates that even after four cycles, the Fe_2O_3/Fe_3O_4 nanocomposite catalyst maintained a significant level of performance, demonstrating its reusability. After each cycle of the reaction, the rate of degradation slowed slightly, suggesting that some iron oxide was being leached out of solution or aggregating.

2.8. Application in Photodegrading Dye-Enriched Lake Water

To add realism and demonstrate the viability of the developed Fe_2O_3/Fe_3O_4 nanocomposite, the photocatalytic degradation of two dyestuffs, MB and PY, was studied in samples taken from Dumat Aljandal Lake, a lake in the Aljouf region of Saudi Arabia. The working system was 100 mL of lake water containing a mixture of MB (20 ppm) and PY (20 ppm), in which 20 mg of Fe_2O_3/Fe_3O_4 catalyst was ultrasonicated and H_2O_2 (20 mg L^{-1}) was added. This mixture was left in the dark to address adsorption equilibrium. After that, the photocatalytic reaction was conducted under solar illumination where the PY and MB residues were spectrophotometrically recorded at λ_{max} 546 nm and 663 nm, respectively. As shown in Figure 7A, the absorbance of PY and MB in the UV–visible range decreases as the illumination time reaches 85 min. The performance of the photocatalytic degradation of MB and PY amounts to 70.8% and 92.7%, respectively (Figure 7B). These fascinating results show

that the synthesized Fe_2O_3/Fe_3O_4 nanocomposite is highly effective in photodegrading dyes that contaminated natural water sources.

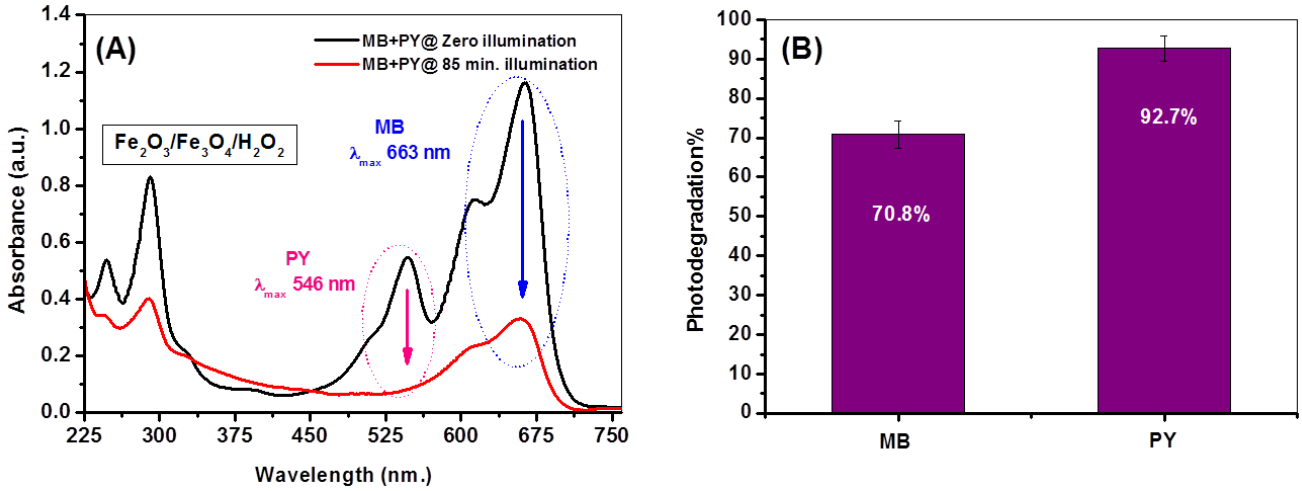

Figure 7. The absorption spectra of a mixture of MB and PY dyestuff mixture before and after solar-driven photo-Fenton catalytic degradation in presence of $Fe_2O_3/Fe_3O_4/H_2O_2$ hybrid catalyst. (**A**) Comparison of the photodegradation efficiency of MB and PY in their mixture in presence of $Fe_2O_3/Fe_3O_4/H_2O_2$ hybrid catalyst (**B**).

2.9. Plausible Mechanism for the Photocatalytic Degradation Process

The catalytic mechanism for the solar-driven photo-Fenton degradation of MB in presence of the biosynthesized Fe_2O_3/Fe_3O_4 nanocomposite is shown in Figure 8. At first, the developed Fe_2O_3/Fe_3O_4 nanocomposite can efficiently absorb photons from solar light forming photogenerated electron–hole pairs, and Equation (3) shows the band gap energy of the nanocomposite is 2.92 eV. The photogenerated electrons and holes could react with H_2O_2 and H_2O, respectively, to produce $^{\bullet}OH/^{-}OH$ species, see Equations (4) and (5). Also, the photogenerated holes could react with ^{-}OH to produce $^{\bullet}OH$ radicals, see Equation (6). Notably, excited electrons have the potential to reduce the Fe(III) on the Fe_2O_3 particulates to Fe(II). Subsequently, Fe(II) could react with H_2O_2 to form the Fenton system, leading to the generation of $^{\bullet}OH$ radicals. Note that due to the high conductivity of Fe_3O_4, certain Fe_3O_4 particulates may serve as a conduit for the photogenerated electrons and holes to travel along the surface of the nanocomposite, significantly reducing the probability of their recombination [47]. This will result in more electrons and holes forming reactive species that could be engaged in the photodegradation of MB. This photo-Fenton system relies on reactive species, specifically $^{\bullet}OH$ and h^+ that all act as reactive species exhibiting a pivotal role in photomineralizing MB, see Equation (7).

$$Fe_2O_3/Fe_3O_4\ NPs + h\upsilon \longrightarrow Fe_2O_3/Fe_3O_4\ NPs\ (e^-_{CB} + h^+_{VB}) \quad (3)$$

$$H_2O_2 + Fe_2O_3/Fe_3O_4NPs(e^-_{CB}) \longrightarrow {}^{\bullet}OH + {}^{-}OH \quad (4)$$

$$H_2O + Fe_2O_3/Fe_3O_4NPs(h^+_{vb}) \longrightarrow {}^{\bullet}OH + {}^{-}OH \quad (5)$$

$$Fe_2O_3/Fe_3O_4NPs(h^+_{vb}) + {}^{-}OH \longrightarrow {}^{\bullet}OH \quad (6)$$

$$MB + {}^{\bullet}OH/h^+_{vb} \longrightarrow \text{Degradation products } (CO_2 + H_2O) \quad (7)$$

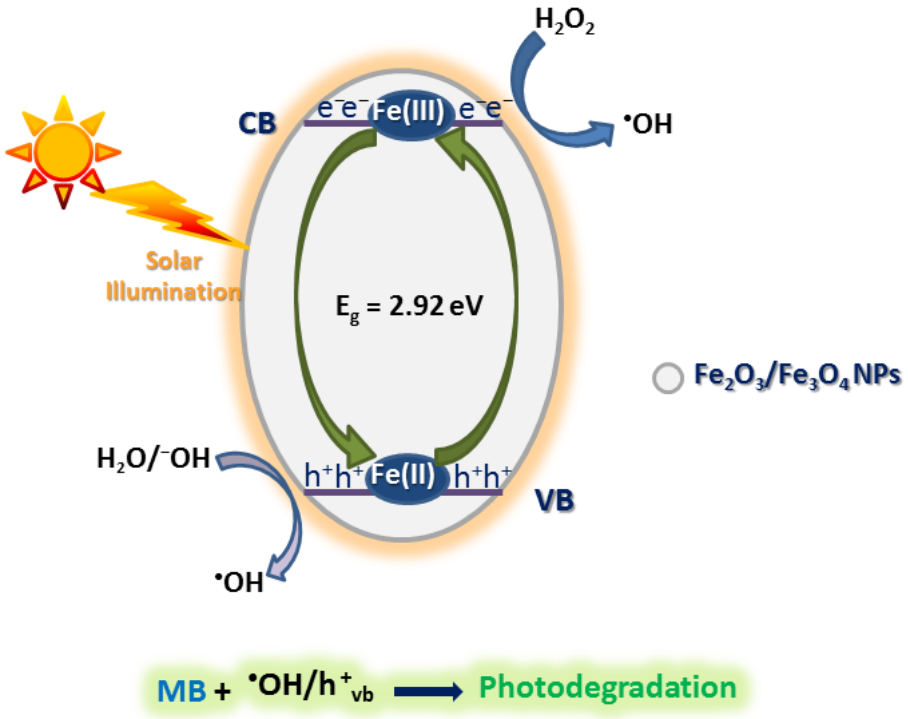

Figure 8. A plausible mechanism for the solar-driven photo-Fenton degradation of MB in presence of biosynthesized Fe_2O_3/Fe_3O_4 nanocomposite.

3. Materials and Methods

3.1. Materials

Leaves of guajava were taken from one of the farms in Egypt's Fayoum governorate. Methylene blue was obtained from Merck. Pyronine Y, ferric nitrate nonahydrate (>98%), ethanol, and H_2O_2 were purchased from Sigma-Aldrich. All of the reagents and chemicals have been utilized exactly as they were received, with no further purification. During the preparation, bi-distilled water was used.

3.2. Methods

3.2.1. Preparation of Guajava Leaves Aqueous Extract

After collecting the leaves of guajava, they were washed in tap water and then bi-distilled water before being dried in the shade for three weeks. The aqueous extract of guajava leaves was made by first rinsing 10 g of the leaves with bi-distilled water, and then boiling the leaves in 100 mL of bi-distilled water at 70 °C for 25 min. After filtering out any remaining leaf fragments, the remaining extract was used as a stabilizing, capping, and reducing agent in the production of iron oxide nanoparticles.

3.2.2. Preparation of Iron Oxide Nanoparticles Using Guajava Leaves Aqueous Extract

Ferric nitrate nonahydrate (4.0 g) was dissolved in 100 mL of aqueous extract of guajava leaves/bi-distilled water mix (v/v = 1/2). For 4.0 h, the above solution was heated to 80 °C while stirring constantly. After an hour of phyto-mediated reaction, the color of working solution darkened. The color shift may be owing to the formation of iron oxide. After separating the solids, they were washed three times in ethanol, then in bi-distilled water before being dried at 250 °C for 12 h.

3.2.3. Photocatalytic Experiments

The photocatalytic activity of the phytosynthesized iron oxide nanocomposite was examined by calculating the rate of breakdown of the ubiquitous MB dye. Initial testing showed that the catalytic system could handle concentrations of MB in aqueous solution

(20 mg/L) that were higher than those reported in the majority of the previous studies in the literature. A typical methodology entails ultrasonicating 20 mg of the developed iron oxide nanocomposite with (100 mL) of MB for 5 min in the presence of 20 mg L^{-1} H_2O_2 (at natural pH). Then, the concoction was left to stir in the dark for 30 min at room temperature so that the MB could adsorb to the catalyst surface at equilibrium. After that, 760 W/m^2 of solar irradiance (as determined by a pyranometer) was shone on it. After centrifuging about 5 mL of the mixed solution at a certain illumination time, the absorbance of the MB clear solution at λ_{max} 663 nm was measured to determine the photodegradation efficiency. A pure Fe_2O_3/Fe_3O_4 nanocomposite or H_2O_2 homogenous catalyst was used in a photodegradation suit as a control test.

3.3. Instrumental

The analysis of X-ray diffraction was performed utilizing D/Max2500VB2+/Pc X-ray diffractometer (Rigaku Company, Tokyo, Japan) within detector of Cu of 1.54 Å wavelength. Thermal gravimetric analysis (TGA) measurement was conducted using Shimadzu TGA-51 analyzer. FTIR readings were taken using a Shimadzu (Tokyo, Japan) IR Tracer-100 spectrophotometer. The Brunauer–Emmett–Teller (BET) equation and Barrett–Joyner–Halenda (BJH) technique were used to assess the surface area and pore size distribution. Sample morphology was recorded via JEOL, JEM-2100 electron microscopy (Tokyo, Japan). Absorption spectroscopic measurements were monitored in the UV-Vis range using Agilent Cary 60 spectrophotometer. Using a Phoenix (Blomberg, Germany) 8000 Analyzer, the total organic carbon (TOC) was measured to assess the efficacy of the dye photomineralization procedure.

4. Conclusions

In conclusion, a facile one-pot phyto-mediated avenue was successfully employed to prepare a binary Fe_2O_3/Fe_3O_4 heterostructure. XRD and SEM characterizations addressed the porous morphology of the prepared composite in which Fe_2O_3 of average crystallite size 8.43 nm was successfully mixed with plate-like aggregates of Fe_3O_4 of 15.1 nm average crystallite size. FTIR analysis displayed the distinct Fe-O assignments. EDX and elemental mapping indicated highly intense peaks of iron and oxygen verifying high purity of the composite with highly symmetrical and uniform distribution as revealed from elemental mapping. The prepared Fe_2O_3/Fe_3O_4 binary nanocomposite is thermally stable. The isotherm of Fe_2O_3/Fe_3O_4 nanocomposite catalyst shows slit-shaped pores in loose particulates in plate-like aggregates and a mesoporous pore size distribution which are consistent with SEM imaging morphology. The optical properties of the catalyst reveal a narrow band gap (2.92 eV) that efficiently absorbs visible photons of solar light. Moreover, the solar-driven photo-Fenton catalytic activity of the constructed Fe_2O_3/Fe_3O_4 heterostructure in photodegrading MB that was investigated in the presence of H_2O_2 illustrates superior activity. This photo-Fenton system provided the highest rate constant (0.0143 min^{-1}) and superior activity in degrading MB by 7.15 times greater than Fe_2O_3/Fe_3O_4 or H_2O_2 alone. The Fe_2O_3/Fe_3O_4 nanocomposite catalyst performed well after four solar-driven photo-Fenton photodegradation cycles, proving its reusability. This anticipates the synergism between the developed heterostructure in delimiting the electron–hole recombination and H_2O_2 oxidizing agent to generate a higher density of reactive oxidizing species. Furthermore, when using a combination of MB and pyronine Y (PY) dyestuffs, the Fe_2O_3/Fe_3O_4 nanocomposite demonstrated high dye photodegradation efficiencies in the subsequent photocatalytic remediation of polluted lake water.

Author Contributions: Conceptualization, A.A.E. and A.E.-N.I.E.; methodology, A.A.E.; software, T.H.A.H., M.F.H. and E.F.E.A.; validation, A.E.-N.I.E., E.F.E.A. and M.F.H.; formal analysis, A.A.E.; investigation, T.H.A.H. and A.E.-N.I.E.; resources, A.A.E. and T.H.A.H. data curation, A.A.E., E.F.E.A. and M.F.H.; writing—original draft preparation, A.A.E.; writing—review and editing, A.A.E. and A.E.-N.I.E.; visualization, T.H.A.H., M.F.H. and E.F.E.A. supervision, A.A.E. and A.E.-N.I.E.; project administration, A.A.E.; funding acquisition, A.A.E. All authors have read and agreed to the published version of the manuscript.

Funding: This work was funded by the Deanship of Scientific Research at Jouf University under grant number (DSR2022-RG-0133).

Data Availability Statement: The original contributions presented in the study are included in the article, further inquiries can be directed to the corresponding author/s.

Conflicts of Interest: The authors declare no conflicts of interest.

References

1. Lellis, B.; Fávaro-Polonio, C.Z.; Pamphile, J.A.; Polonio, J.C. Effects of textile dyes on health and the environment and bioremediation potential of living organisms. *Biotechnol. Res. Innov.* **2019**, *3*, 275–290. [CrossRef]
2. Caviglia-Harris, J.L.; Kahn, J.R.; Green, T. Demand-side policies for environmental protection and sustainable usage of renewable resources. *Ecol. Econ.* **2003**, *45*, 119–132. [CrossRef]
3. Dehghani, M.H.; Karimi, B.; Rajaei, M.S. The effect of aeration on advanced coagulation, flotation and advanced oxidation processes for color removal from wastewater. *J. Mol. Liq.* **2016**, *223*, 75–80. [CrossRef]
4. Oturan, M.A.; Aaron, J.J. Advanced oxidation processes in water/wastewater treatment: Principles and applications. A review. *Crit. Rev. Environ. Sci. Technol.* **2014**, *44*, 2577–2641. [CrossRef]
5. Show, B.; Mukherjee, N.; Mondal, A. α-Fe_2O_3 nanospheres: Facile synthesis and highly efficient photo-degradation of organic dyes and surface activation by nano-Pt for enhanced methanol sensing. *RSC Adv.* **2016**, *6*, 75347–75358. [CrossRef]
6. Sanad, M.M.S.; Farahat, M.M.; El-Hout, S.I.; El-Sheikh, S.M. Preparation and characterization of magnetic photocatalyst from the banded iron formation for effective photodegradation of methylene blue under UV and visible illumination. *J. Environ. Chem. Eng.* **2021**, *9*, 105127. [CrossRef]
7. Rehman, A.; Daud, A.; Warsi, M.F.; Shakir, I.; Agboola, P.O.; Sarwar, M.I.; Zulfiqar, S. Nanostructured maghemite and magnetite and their nanocomposites with graphene oxide for photocatalytic degradation of methylene blue. *Mater. Chem. Phys.* **2020**, *256*, 123752. [CrossRef]
8. Pirhashemi, M.; Habibi-Yangjeh, A.; Pouran, S.R. Review on the criteria anticipated for the fabrication of highly efficient ZnO-based visible-lightdriven photocatalysts. *J. Ind. Eng. Chem.* **2018**, *62*, 1–25. [CrossRef]
9. Farhadian, N.; Liu, S.; Asadi, A.; Shahlaei, M.; Moradi, S. Enhanced heterogeneous Fenton oxidation of organic pollutant via Fe-containing mesoporous silica composites: A review. *J. Mol. Liq.* **2020**, *321*, 114896. [CrossRef]
10. Luo, X.; Cai, W.; Vimalanathan, K.; Igder, A.; Gardner, Z.; Petticrew, S.; He, S.; Chuah, C.; Tang, Y.; Su, P.; et al. Magnetite Nanoparticle/Copper Phosphate Nanoflower Composites for Fentonlike Organic Dye Degradation. *ACS Appl. Nano Mater.* **2022**, *5*, 2875–2884. [CrossRef]
11. Chen, Y.; Miller, C.J.; Waite, T.D. Heterogeneous Fenton chemistry revisited: Mechanistic insights from ferrihydrite-mediated oxidation of formate and oxalate. *Environ. Sci. Technol.* **2021**, *55*, 14414–14425. [CrossRef] [PubMed]
12. Hashemzadeh, B.; Alamgholiloo, H.; Pesyan, N.N.; Asgari, E.; Sheikhmohammadi, A.; Yeganeh, J.; Hashemzadeh, H. Degradation of ciprofloxacin using hematite/MOF nanocomposite as a heterogeneous fenton-like catalyst: A comparison of composite and core−shell structures. *Chemosphere* **2021**, *281*, 130970. [CrossRef] [PubMed]
13. Sujay Shekar, G.C.; Alkanad, K.; Hezam, A.; Alsalme, A.; Al-Zaqri, N.; Lokanath, N.K. Enhanced photo-Fenton activity over a sunlight-driven ignition synthesized α-Fe_2O_3-Fe_3O_4/CeO_2 heterojunction catalyst enriched with oxygen vacancies. *J. Mol. Liq.* **2021**, *335*, 116186. [CrossRef]
14. Kaushik, J.; Twinkle; Tisha; Nisha; Baig, A.; Sonal; Dubey, P.; Sonkar, S.K. Photoactive Fe_3O_4@Fe_2O_3 Synthesized from Industrial Iron Oxide Dust for Fenton-Free Degradation of Multiple Organic Dyes. *Ind. Eng. Chem. Res.* **2023**, *62*, 10487–10497. [CrossRef]
15. Kaushik, J.; Twinkle; Anand, S.R.; Choudhary, S.K.; Sonkar, S.K. H_2O_2-Free Sunlight-Promoted Photo-Fenton-Type Removal of Hexavalent Chromium Using Reduced Iron Oxide Dust. *ACS EST Water* **2023**, *3*, 227–235. [CrossRef]
16. Alrowaili, Z.A.; Alsohaimi, I.H.; Betiha, M.A.; Essawy, A.A.; Mousa, A.A.; Alruwaili, S.F.; Hassan, H.M.A. Green fabrication of silver imprinted titania/silica nanospheres as robust visible light-induced photocatalytic wastewater purification. *Mater. Chem. Phys.* **2020**, *241*, 122403. [CrossRef]
17. Essawy, A.A. Silver imprinted zinc oxide nanoparticles: Green synthetic approach, characterization and efficient sunlight-induced photocatalytic water detoxification. *J. Clean. Prod.* **2018**, *183*, 1011–1020. [CrossRef]
18. Herney-Ramirez, J.; Vicente, M.A.; Madeira, L.M. Heterogeneous photo-Fenton oxidation with pillared clay-based catalysts for wastewater treatment: A review. *Appl. Catal. B* **2010**, *98*, 10–26. [CrossRef]
19. Cassano, D.; Zapata, A.; Brunetti, G.; Del Moro, G.; Di Iaconi, C.; Oller, I.; Mascolo, G. Comparison of several combined/integrated biological-AOPs setups for the treatment of municipal landfill leachate: Minimization of operating costs and effluent toxicity. *Chem. Eng. J.* **2011**, *172*, 250–257. [CrossRef]
20. Muñoz, I.; Malato, S.; Rodríguez, A.; Domènech, X. Integration of environmental and economic performance of processes. Case study on advanced oxidation processes for wastewater treatment. *J. Adv. Oxid. Technol.* **2008**, *11*, 270–275. [CrossRef]
21. Clarizia, L.; Russo, D.; Di Somma, I.; Marotta, R.; Andreozzi, R. Homogeneous photo-Fenton processes at near neutral pH: A review. *Appl. Catal. B* **2017**, *209*, 358–371. [CrossRef]

22. Gallard, H.; De Laat, J. Kinetic modelling of Fe (III)/H_2O_2 oxidation reactions in dilute aqueous solution using atrazine as a model organic compound. *Water Res.* **2000**, *34*, 3107–3116. [CrossRef]
23. Essawy, A.A.; Aleem, S.A.E. Physico-mechanical properties, potent adsorptive and photocatalytic efficacies of sulfate resisting cement blends containing micro silica and nano-TiO_2. *Constr. Build. Mater.* **2014**, *52*, 1–8. [CrossRef]
24. Sahoo, D.; Shakya, J.; Ali, N.; Yoo, W.J.; Kaviraj, B. Edge Rich Ultrathin Layered MoS_2 Nanostructures for Superior Visible Light Photocatalytic Activity. *Langmuir* **2022**, *38*, 1578–1588. [CrossRef] [PubMed]
25. Twinkle; Kaushik, J.; Singla, T.; Lamba, N.K.; Jain, M.; Sharma, N.; Choudhary, S.K.; Sonkar, S.K. Fe_3O_4 Nanoparticles Synthesized from Waste Iron Dust for Sunlight-Boosted Photodegradation of Nitrophenols and Their Mixtures. *Ind. Eng. Chem. Res.* **2023**, *62*, 9091–9103. [CrossRef]
26. Si, J.-C.; Xing, Y.; Peng, M.-L.; Zhang, C.; Busk, N.; Chen, C.; Cui, Y.-L. Solvothermal synthesis of tunable iron oxide nanorods and their transfer from organic phase to water phase. *CrystEngComm* **2014**, *16*, 512–516. [CrossRef]
27. Rajakaruna, T.P.B.; Udawatte, C.P.; Chandrajith, R.; Rajapakse, R.M.G. Formulation of Iron Oxide and Oxy-hydroxide Nanoparticles from Ilmenite Sand through a Low Temperature Process. *ACS Omega* **2021**, *6*, 17824–17830. [CrossRef] [PubMed]
28. Nag, S.; Roychowdhury, A.; Das, D.; Mukherjee, S. Synthesis of α-Fe_2O_3-functionalised graphene oxide nanocomposite by a facile low temperature method and study of its magnetic and hyperfine properties. *Mater. Res. Bull.* **2016**, *74*, 109–116. [CrossRef]
29. Chernyshova, I.V.; Hochella, M.F., Jr.; Madden, A.S. Size-dependent structural transformations of hematite nanoparticles. 1. Phase transition. *Phys. Chem. Chem. Phys.* **2007**, *9*, 1736–1750. [CrossRef]
30. Zheng, L.; Su, W.; Qi, Z.; Xu, Y.; Zhou, M. First-order metal–insulator transition and infrared identification of shape-controlled magnetite nanocrystals. *Nanotechnology* **2011**, *22*, 485706. [CrossRef]
31. Yao, L.; Chen, Z.; Li, J.; Shi, C. Creation of oxygen vacancies to activate lanthanum doped bismuth titanate nanosheets for efficient synchronous photocatalytic removal of Cr(VI) and methyl orange. *J. Mol. Liq.* **2020**, *314*, 113613. [CrossRef]
32. Murillo-Sierra, J.C.; Maya-Treviño, M.D.L.; Nuñez-Salas, R.E.; Pino-Sandoval, D.A.; Hernández-Ramírez, A. Facile synthesis of ZnS/WO3 coupled photocatalyst and its application on sulfamethoxazole degradation. *Ceram. Int.* **2022**, *48*, 13761–13769. [CrossRef]
33. Zhao, X.; Wang, R.; Lu, Z.; Wang, W.; Yan, Y. Dual sensitization effect and conductive structure of Fe_3O_4@mTiO_2/C photocatalyst towards superior photodegradation activity for bisphenol A under visible light. *J. Photochem. Photobiol. A Chem.* **2019**, *382*, 111902. [CrossRef]
34. Essawy, A.A.; Alsohaimi, I.H.; Alhumaimess, M.S.; Hassan, H.M.A.; Kamel, M.M. Green synthesis of spongy Nano-ZnO productive of hydroxyl radicals for unconventional solar-driven photocatalytic remediation of antibiotic enriched wastewater. *J. Environ. Manag.* **2020**, *271*, 110961. [CrossRef] [PubMed]
35. Abu-Dief, A.M.; Essawy, A.A.; Diab, A.K.; Mohamed, W.S. Facile synthesis and characterization of novel Gd_2O_3–CdO binary mixed oxide nanocomposites of highly photocatalytic activity for wastewater remediation under solar illumination. *J. Phys. Chem. Solids* **2021**, *148*, 109666. [CrossRef]
36. Essawy, A.A.; Abdel-Farid, I.B. Hybrid solvothermal/sonochemical-mediated synthesis of ZnO NPs generative of •OH radicals: Photoluminescent approach to evaluate •OH scavenging activity of Egyptian and Yemeni Punica granatum arils extract. *Ultrason. Sonochem.* **2022**, *89*, 106152. [CrossRef] [PubMed]
37. Tahir, M.; e-Alam, M.F.; Atif, M.; Mustafa, G.; Ali, Z. Investigation of optical, electrical and magnetic properties of hematite α-Fe_2O_3 nanoparticles via sol-gel and co-precipitation method. *J. King Saud Univ. Sci.* **2023**, *35*, 102695. [CrossRef]
38. Ozer, Z.N.; Ozkan, M.; Pat, S. Optical and electric properties of Fe_3O_4 nanoparticle doped ZnO thin films. *Ceram. Int.* **2024**, *50*, 22696–22703. [CrossRef]
39. Essawy, A.A.; Nassar, A.M.; Arafa, W.A.A. A novel photocatalytic system consists of Co(II) complex@ ZnO exhibits potent antimicrobial activity and efficient solar-induced wastewater remediation. *Sol. Energy* **2018**, *170*, 388–397. [CrossRef]
40. Essawy, A.A.; Sayyah, S.M.; El-Nggar, A.M. Ultrasonic-mediated synthesis and characterization of TiO_2-loaded chitosan-grafted-polymethylaniline nanoparticles of potent efficiency in dye uptake and sunlight driven self-cleaning applications. *RSC Adv.* **2016**, *6*, 2279–2294. [CrossRef]
41. Jiang, X.; Li, L.; Cui, Y.; Cui, F. New branch on old tree: Green-synthesized RGO/Fe_3O_4 composite as a photo-Fenton catalyst for rapid decomposition of methylene blue. *Ceram. Int.* **2017**, *43*, 14361–14368. [CrossRef]
42. Liu, Y.; Jin, W.; Zhao, Y.; Zhang, G.; Zhang, W. 2017. Enhanced catalytic degradation of methylene blue by α-Fe_2O_3/graphene oxide via heterogeneous photo-Fenton reactions. *Appl. Catal. B* **2017**, *206*, 642–652. [CrossRef]
43. Quynh, H.G.; Kiet, N.A.; Thanh, H.V.; Tue, T.M.; Phuong, N.T.T.; Long, N.Q. Removal of aqueous organic pollutant by photo-Fenton process using low-cost Fe3O4/zeolite A. *IOP Conf. Ser. Earth Environ. Sci.* **2021**, *947*, 012013. [CrossRef]
44. Huang, C.-W.; Hsu, S.-Y.; Lin, J.-H.; Jhou, Y.; Chen, W.-Y.; Lin, K.-Y.A.; Lin, Y.-T.; Nguyen, V.-H. Solar-light-driven $LaFe_xNi_{1-x}O_3$ perovskite oxides for photocatalytic Fenton-like reaction to degrade organic pollutants. *Beilstein J. Nanotechnol.* **2022**, *13*, 882–895. [CrossRef] [PubMed]
45. Wang, N.; Zheng, T.; Zhang, G.; Wang, P. A review on Fenton like processes for organic wastewater treatment. *J. Environ. Chem. Eng.* **2016**, *4*, 762–787. [CrossRef]

46. Zazo, J.A.; Pliego, G.; Blasco, S.; Casas, J.A.; Rodriguez, J.J. Intensification of the Fenton process by increasing the temperature. *Ind. Eng. Chem. Res.* **2011**, *50*, 866–870. [CrossRef]
47. Wang, Z.; Fan, Y.; Wu, R.; Huo, Y.; Wu, H.; Wang, F.; Xu, X. Novel magnetic g-C3N4/α-Fe2O3/Fe3O4 composite for the very effective visible-light-Fenton degradation of Orange II. *RSC Adv.* **2018**, *8*, 5180. [CrossRef]